ADVANCED OPTICAL MATERIALS

Supporting Information

for *Adv. Optical Mater.*, DOI 10.1002/adom.202500236

High-Efficiency Multi-Level Beam Switching with Single-Gate Tunable Metasurfaces Based on Graphene

*Juho Park, Ju Young Kim, Sunghyun Nam and Min Seok Jang**

Supplementary Information

High-efficiency multi-level beam switching with single-gate tunable metasurfaces based on graphene

Juho Park[1], Ju Young Kim[1], Sunghyun Nam[1], and Min Seok Jang[1*]

[1]School of Electrical Engineering, Korea Advanced Institute of Science and Technology, Daejeon 34141, Republic of Korea

*Corresponding author. Min Seok Jang: jang.minseok@kaist.ac.kr

S1. Gate voltage vs Fermi level

We used the capacitor model [1] to estimate the required gate voltages to reach certain Fermi levels of graphene. It turns out a gate voltage with a difference of 25 V from the Dirac voltage is needed to achieve a Fermi level of 1.0 eV.

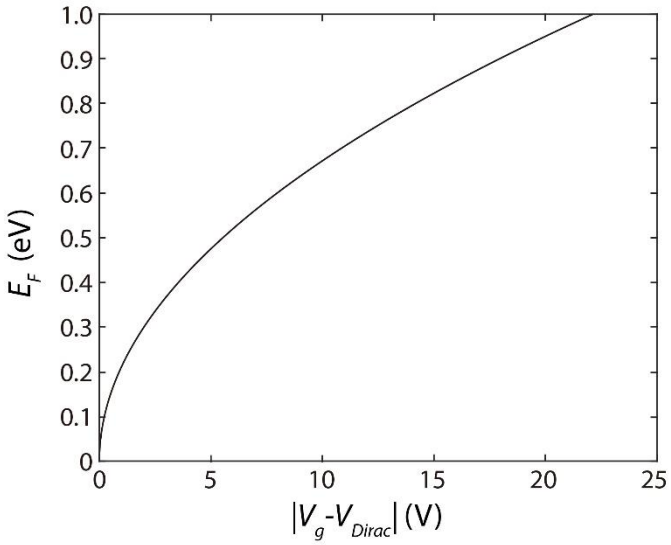

Figure S1. Dependence of graphene Fermi level as a function of gate voltage.

S2. Adjoint gradient formulation

Adjoint method is an efficient tool for calculating gradients with respect to design parameters. It is vastly used for many photonic inverse design applications. Adjoint method needs forward and adjoint (backward) simulations for calculating the gradient. For beam deflecting applications, the forward simulation is needed to evaluate the diffraction efficiency and the forward electric field E_{for} inside the metagrating region, when the source is an incident plane wave. The adjoint simulation is needed to evaluate the adjoint electric field E_{adj} when the source is a backward incident plane wave from the desired target direction. In this work, we utilize the shape-derivative version of the adjoint method to avoid additional binarization procedures, otherwise needed for grayscale permittivity gradient.

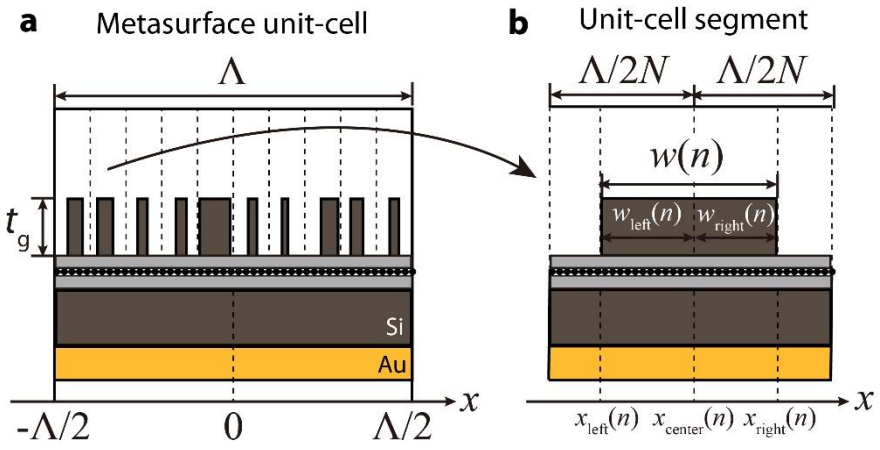

Figure S2. (a) Metasurface unit-cell and (b) unit-cell segment. The width of unit-cell segment drawn in **(b)** is exaggerated to illustrate parametrizations for shape-derivative.

To implement free-form optimizations using shape-derivatives, we first divide the metasurface unit-cell into $N = 10$ segments having equidistant widths, and place one Si pillar for each segment (**Fig. S2a**). And to make the Si pillar move freely inside each segment, we parametrize the left and right widths from the center of segment as follows (**Fig. S2b**):

$$w_{\text{left}}(n) = p_{\text{left}}(n)\frac{\Lambda}{2N}, \quad w_{\text{right}}(n) = p_{\text{right}}(n)\frac{\Lambda}{2N},$$

$$w(n) = w_{\text{left}}(n) + w_{\text{right}}(n), \quad n = 1, 2, \ldots, N,$$

where $p_{\text{left}}(n)$ and $p_{\text{right}}(n)$ represent normalized left and right widths of Si pillars. By

setting the range of the normalized left and right widths between zero and unity, one can represent any Si pillar shape inside the segment. The *x*-coordinates of the center point and both edges of the Si pillar are represented as follows:

$$x_{\text{center}}(n) = \frac{\Lambda}{2N}(-N + 2n - 1),$$

$$x_{\text{left}}(n) = x_{\text{center}}(n) - w_{\text{left}}(n), \;\; x_{\text{right}}(n) = x_{\text{center}}(n) + w_{\text{right}}(n)$$

Using the notations above, we get the adjoint gradient formulation as follows [2]:

$$\frac{\partial FoM}{\partial \boldsymbol{p}} = \frac{t_g \Lambda}{2N}\{[\epsilon_{Si} - \epsilon_{Air}][E_{for}^{||}(\boldsymbol{x}(\boldsymbol{p})) \cdot E_{adj}^{||}(\boldsymbol{x}(\boldsymbol{p})) + \frac{1}{\epsilon_{Si}\epsilon_{Air}} \cdot D_{for}^{\perp}(\boldsymbol{x}(\boldsymbol{p})) \cdot D_{adj}^{\perp}(\boldsymbol{x}(\boldsymbol{p}))]\}$$

where $E_{for}^{||}$, $E_{adj}^{||}$ represent forward and adjoint fields parallel to the boundary of the pillars, respectively, $D_{for}^{\perp}$, $D_{adj}^{\perp}$ represent forward and adjoint displacement fields perpendicular to the boundary of the pillars, respectively, and $\boldsymbol{x}(\boldsymbol{p})$ is a vector of the locations of the left and the right boundaries of the pillar, and $\boldsymbol{p}$ is a vector of normalized left and right widths of the Si pillars.

S3. Metagrating layer and substrate thickness sweep analysis

In this section, we report the thickness sweep results (**Fig. S3**) for metagrating and substrate thicknesses, represented as t_g and t_s in **Fig. 1** in the main script. Sweep ranges for both thicknesses are $k_{Si}t_g$ = π/8 ~ 2π and $k_{Si}t_s$ = π/8 ~ 2π, with steps of π/8. At each thickness pair ($k_{Si}t_g$, $k_{Si}t_s$), we conduct 5 optimizations and selected the optimized design having the maximum value of minimum directivities of all orders. We highlight the data points with over 90% minimum directivities, and draw average diffraction efficiencies for those data points. For both two- and three-level beam switching metasurfaces, designs with high directivities were achieved near ($k_{Si}t_g$, $k_{Si}t_s$) = (3π/2, 3π/2). This concentration is more evident for the three-level case. For the four-level switching optimization, we could not achieve designs that displayed over 90% minimum directivities. Interestingly, we observed there is a "forbidden zone" where directivities are low for all three metasurfaces, indicated by red lines in **Fig. S3**. We suspect that the reason for this forbidden zone is possibly due to the Salisbury-screen effect that reduces direct reflection of normally incident waves. A Salisbury screen is one of the antireflection technologies used to eliminate incident waves [3]. It operates on the similar mechanism used for antireflection coatings, based on inducing a π phase shift between the incident wave and the reflected wave, allowing for destructive interference. Here it is desirable to represent phase shifts due to the metagrating and the substrate into $\Delta\phi_{MG} = k_{Si}t_g$ and $\Delta\phi_{Sub} = k_{Si}t_s$. Considering that in our metasurface setup the round-trip phase shift between the incident and the outgoing wave from the metasurface is approximately $2k_{Si}(t_g + t_s) = 2(\Delta\phi_{MG} + \Delta\phi_{Sub})$ (ignoring the phase shift from the graphene and the Si_3N_4 spacer), the antireflection will occur at $\Delta\phi_{MG} + \Delta\phi_{Sub} = (2n + 1)\pi/2$, where n is a non-negative integer. For zone #1 (n = 0), a one-way phase shift due to the metasurface is below π/2, i.e. $\Delta\phi_{MG} + \Delta\phi_{Sub} \leq \pi/2$ and $\Delta\phi_{Sub} \leq \pi/2$. Here, the condition for antireflection is not met, and directivities of the optimized metasurfaces are low. If we increase $\Delta\phi_{MG}$ while fixing $\Delta\phi_{Sub}$, i.e. $\Delta\phi_{MG} + \Delta\phi_{Sub} \geq \pi/2$ and $\Delta\phi_{Sub} \leq \pi/2$, the condition is met and the primary objective is achieved, and the remainder of the freedom in the design parameter space seemed to be devoted to the beam shaping of the other diffraction channels. This phenomenon may be related to forming more suitable Bloch modes resident in the metagrating region, having a larger outcoupling to target diffraction channels, as reported in [4]. For zone #2 (n = 1), the range of $\Delta\phi_{Sub}$ becomes $\pi/2 \leq \Delta\phi_{Sub} \leq 3\pi/2$, unable to satisfy the first phase matching condition (n

= 0). Therefore, the directivities remain low until the second phase matching condition $\Delta\phi_{\mathrm{MG}} + \Delta\phi_{\mathrm{Sub}} = 3\pi/2$ is satisfied. When $\Delta\phi_{\mathrm{MG}}$ is increased to match the second phase matching condition and beyond, again for the same reason, directivities improve. Consequently, these periodic phase matching conditions form a sawtooth pattern enclosing Forbidden zones, shown in **Fig. S3**.

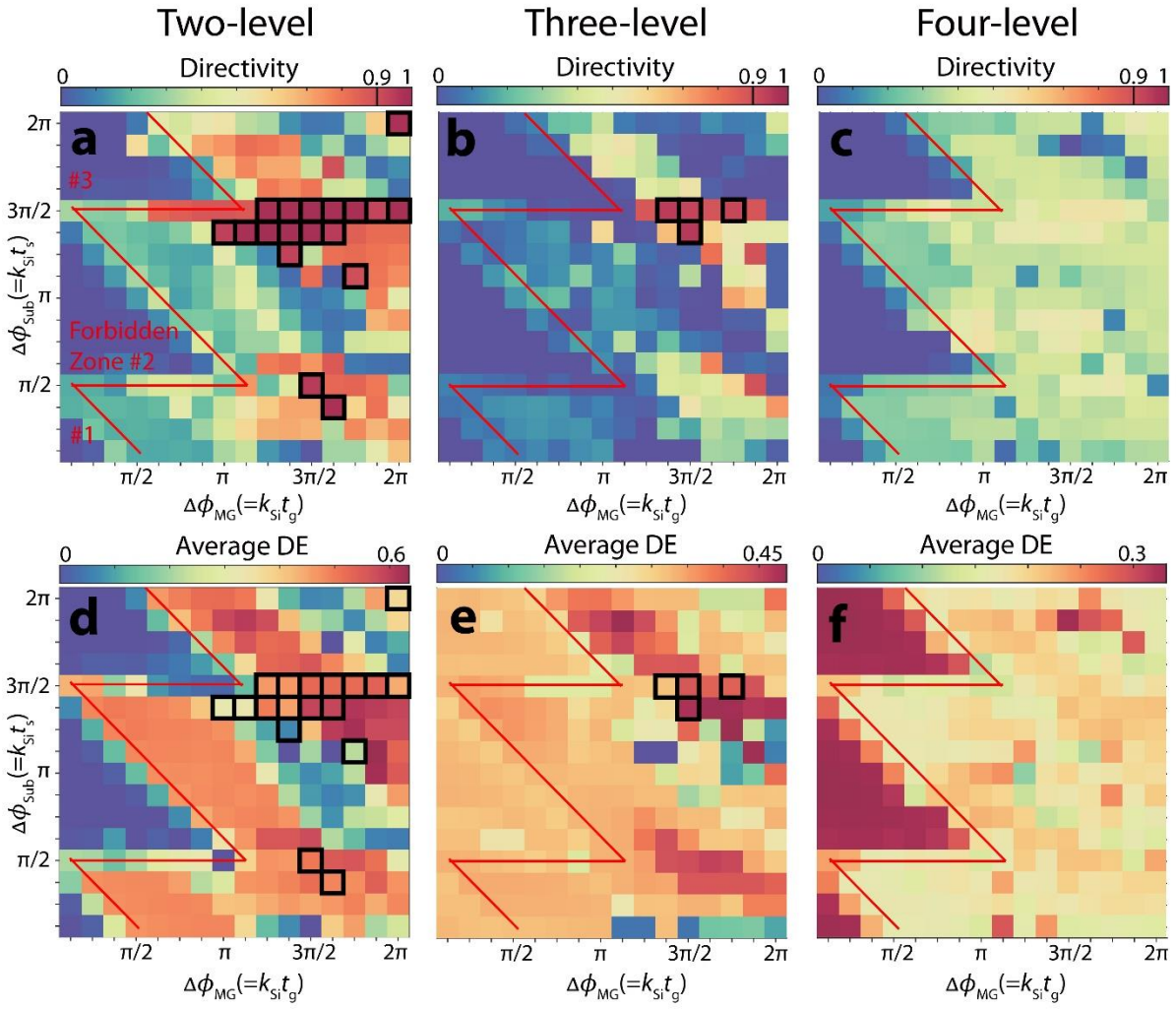

Figure S3. Thickness sweep results for directivity and average diffraction efficiency for optimized **(a, d)** two-, **(b, e)** three-, and **(c, f)** four-level beam switching metasurfaces**.** Data points enclosed with solid squares represent the optimized designs with over 90% directivities. The "forbidden zone" for low directivities is indicated by red lines.

S4. Inverse-designed metagrating patterns of the metasurfaces

We tabulate the left edge locations and widths of the Si metagrating using the variables illustrated in **Fig. S2b**. Note that for the two- and three-level switching metasurfaces, the unit-cell period is $\lambda_0/\sin(80°)$ = 8.123 μm and N = 10. For the four-level switching metasurface, both the unit-cell period and the number of pillars are doubled.

Table S1. Left edge locations and widths of Si pillars for optimized metagrating patterns.

n	Two-level		Three-level		Four-level	
	$x_{\text{left}}(n)$ (μm)	$w(n)$ (μm)	$x_{\text{left}}(n)$ (μm)	$w(n)$ (μm)	$x_{\text{left}}(n)$ (μm)	$w(n)$ (μm)
1	-3.6577	0.3655	-3.8901	0.4039	-7.8088	0.1922
2	-3.1126	0.2695	-2.9944	0.3821	-7.2122	0.3076
3	-2.6634	0.4777	-2.1206	0.8123	-6.5001	0.1754
4	-1.9591	0.3611	-1.5631	0.2060	-5.3802	0.2466
5	-1.0466	0.8123	-0.5754	0.4217	-4.3924	0.2865
6	0.0128	0.3720	0.4371	0.5482	-3.6976	0.2560
7	0.9557	0.4563	0.8432	0.1754	-2.9315	0.2757
8	1.4922	0.4552	1.7729	0.3069	-2.2206	0.2215
9	2.4799	0.1754	2.9182	0.4959	-1.4698	0.4032
10	3.4676	0.2970	3.6770	0.2932	-0.6436	0.4986
11	N/A				0.1520	0.5137
12					0.8937	0.3197
13					1.6551	0.3569
14					2.5485	0.4319
15					3.3877	0.6128
16					4.0821	0.3726
17					4.9583	0.3539
18					5.7124	0.5187
19					6.5620	0.3874
20					7.4329	0.3414

S5. Graphene permittivity dependence on Fermi level

In this section, we discuss the dependency of the graphene permittivity on the Fermi level E_F. To obtain the permittivity, we first calculate the conductivity of graphene following the derivation based on [5]. Then, the conductivity was converted to isotropic permittivity. The electron mobility values discussed are μ_s = 500, 1000, 1500, 2000 cm^2/V·s. In **Fig. S4**, for $E_F < \hbar\omega/2 \sim 0.0775$eV, the high values of Im$\{\varepsilon_{graphene}\}$ are due to interband transition losses. As E_F increases, more intraband transition takes place, shown in a bulge and a dip in Re$\{\varepsilon_{graphene}\}$ and Im$\{\varepsilon_{graphene}\}$, respectively. After some point around E_F = 0.2 eV, the intraband transition seems to settle in, and Re$\{\varepsilon_{graphene}\}$ exhibits a linear relationship with E_F. Meanwhile, Im$\{\varepsilon_{graphene}\}$ converges to a constant value as E_F increases, but these values decrease with increasing μ_s. The linearity of Re$\{\varepsilon_{graphene}\}$ and the constant values of Im$\{\varepsilon_{graphene}\}$ along E_F lead to linear resonance frequency shifts of eigenmodes with preserved linewidths within our E_F range of interest, explaining the reason for the preserved lineshapes in **Fig. 2c**.

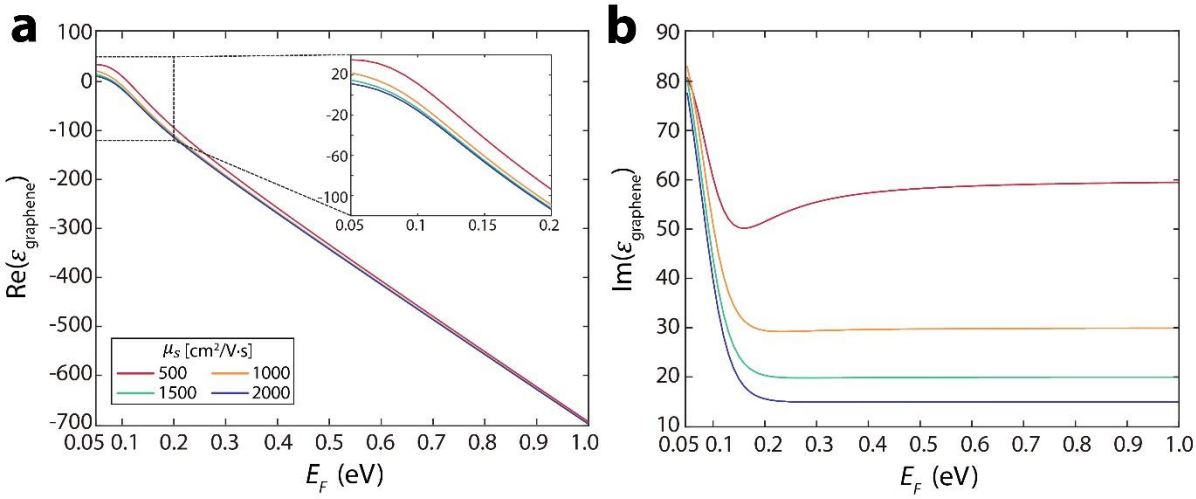

Figure S4. Graphene permittivity dependence on Fermi levels for μ_s = 500, 1000, 1500, 2000 cm^2/V·s.

S6. Riesz Projection method

One way to analyze the relationship between the reflectance/transmittance spectrums with multiple resonances is to utilize temporal coupled-mode theory [6,7] (TCMT). Although TCMT is a general, well-founded multi-port resonator model, we found applying TCMT in our 3-port (=the number of diffraction channels) metasurface system to be difficult, since the 3-by-3 coupling coefficient matrix needed to establish TCMT resulted in too many undetermined variables [8]. For our work, we employ RP methods that yield a clearer analysis for our optical system.

A brief explanation of the Riesz Projection methods is stated hereafter. We define $q(\omega)$ as the analytical continuation of the physical observable of interest. Deploying the Cauchy's residue theorem on $q(\omega)$ and manipulating the contour so that the resonance poles of concern are enclosed by their respective contours, we get the following expansion [9,10]:

$$q(\omega) = \frac{1}{2\pi i}\oint_C \frac{q(\xi)}{\xi - \omega} d\xi = \sum_{m=1}^{M} q_m(r,\omega) + q_{nr}(r,\omega)\,, \text{where}$$

$$q_m(r,\omega) = \frac{-a_m}{\omega_m^{pole} - \omega}, a_m = \frac{1}{2\pi i}\oint_{C_m} q(\xi)d\xi\,, q_{bg}(\omega) = \frac{1}{2\pi i}\oint_{C_{nr}} \frac{q(\xi)}{\xi - \omega} d\xi \qquad (2)$$

Here, the contour C contains inside the frequency of interest ω, but not the pertinent poles. The $q_m(r,\omega)$ embodies the RP onto the eigenspace of each eigenvalue/pole, representing the contribution to the spectrum from each mode. The residues a_m are evaluated along the contours C_m, which involve only one corresponding pole inside. The $q_{bg}(\omega)$ gives the background contribution including the non-resonant effects and the influence of the poles outside the main outer contour C_{nr}.

S7. Full locations of poles and zeros

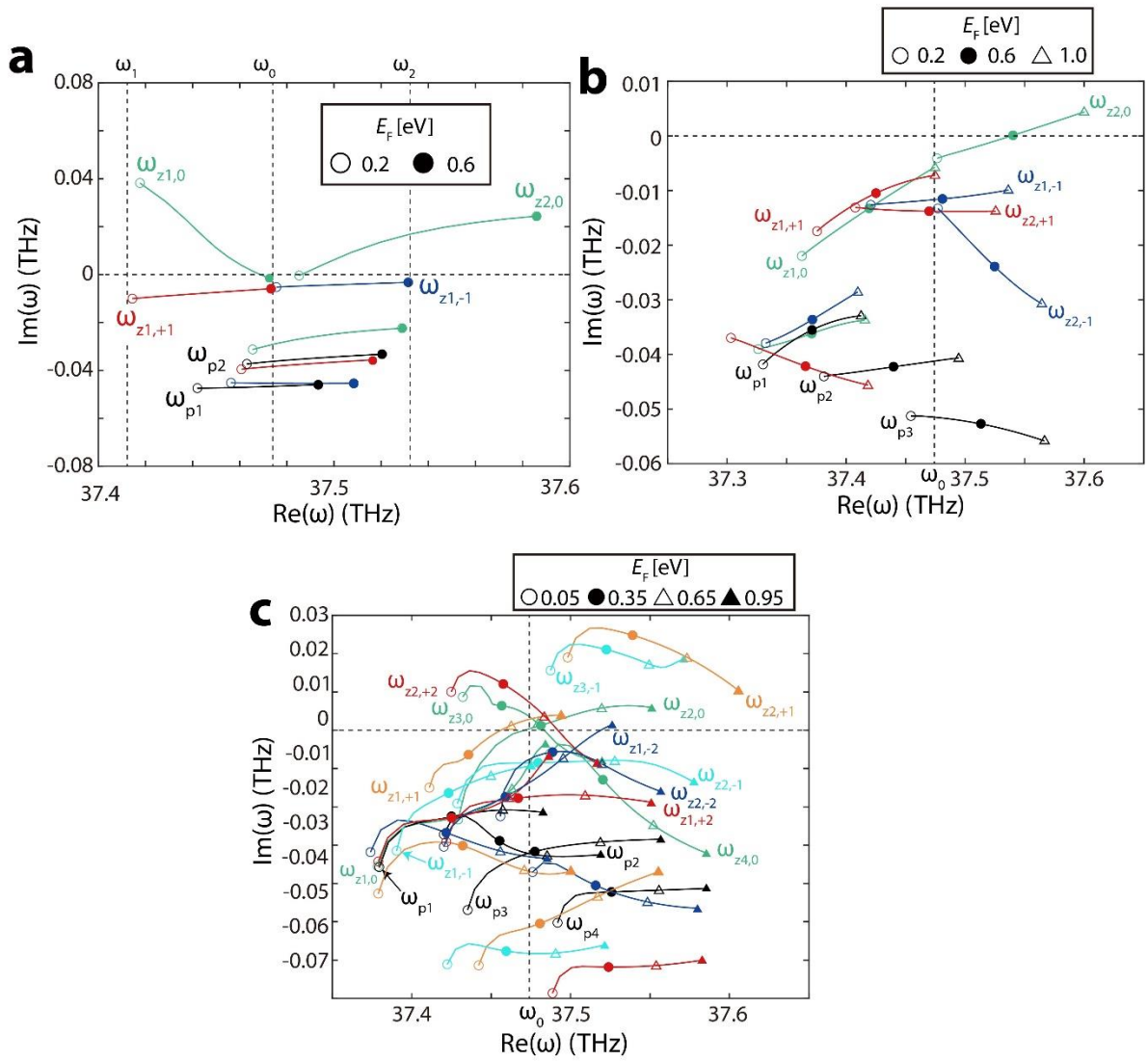

Figure S5. Full representations of poles and zeros of the **(a)** two- **(b)** three- and **(c)** four-level beam switching metasurfaces, corresponding to **(a) Fig. 3a (b) Fig. 4b** and **(c) Fig. 4d** in main text.

S8. QNM electric fields of two-level metasurface

We obtained the QNM eigenmodes' electric field distributions of the two-level switching metasurface using FEM software. There are two poles involved in the switching mechanism of the two-level beam switching metasurface.

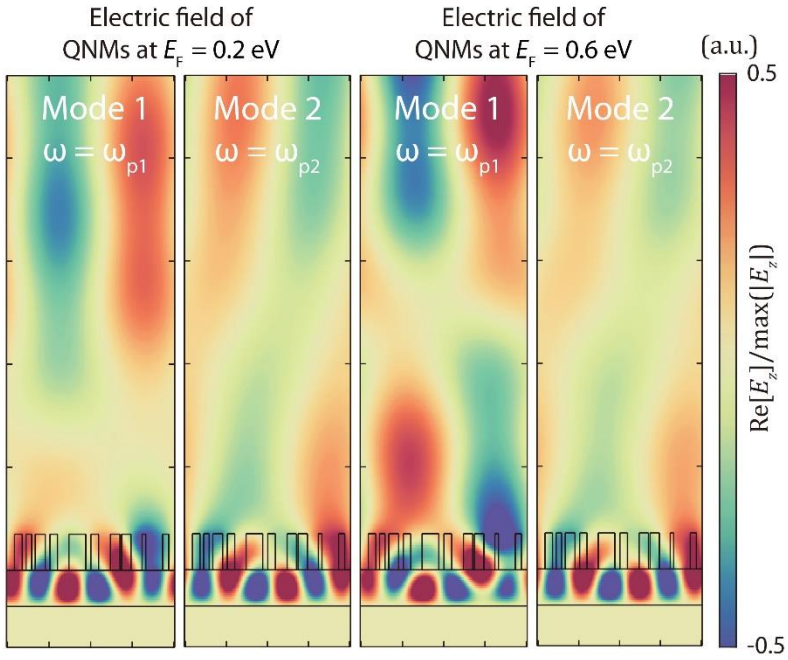

Figure S6. Real part of the electric fields of QNMs at two switching states. Mode 1 corresponds to ω_{p1} and Mode 2 corresponds to ω_{p2}

S9. QNM expansion for two-level metasurface

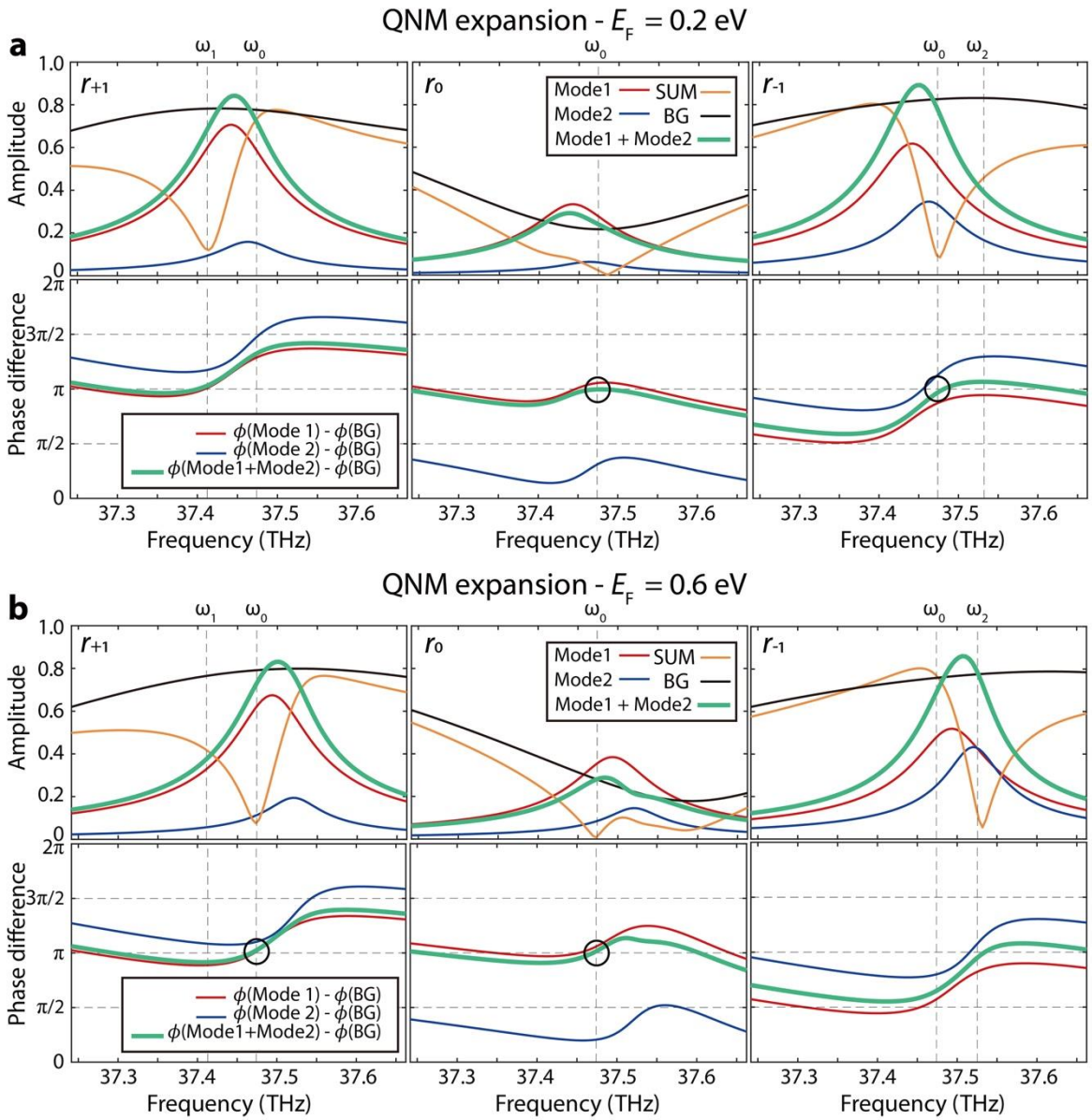

Figure S7. QNM expansion results for the two-level metasurface, showing the amplitude and phase information of the individual modes 1 and 2, their combined mode, and the background mode, for **(a)** E_F = 0.2 eV and **(b)** 0.6 eV.

S10. Beam-switching metasurfaces for additional wavelengths

To give insights on how the beam-switching metasurfaces can be designed to perform at other wavelengths, we report the optimization results for operational wavelengths of λ_0 = 7.0, 7.5, 8.5, and 9.0 μm (the case of 8.0 μm is reported on the manuscript). Note that since the unit-cell period ($\lambda_0/\sin(80°)$), substrate thickness ($k_{Si}t_s$ =3π/2) and metagrating layer thickness ($k_{Si}t_g$=3π/2) are dependent on the wavelengths, they should be altered accordingly. The optimization results on **Table S2** and **S3** show comparable performance to the metasurfaces on the main text, indicating multi-level beam switching metasurfaces can be designed for other wavelengths as well.

Table S2. Directivity and diffraction efficiencies of two-level metasurfaces, optimized for additional wavelengths

λ_0 (μm)	Two-level (E_F = 0.2 and 0.6 eV for +1st and -1st order, respectively)			
	Directivity (+1)	Directivity (-1)	R_{+1}	R_{-1}
7.0	0.9895	0.9875	0.5959	0.5249
7.5	0.9901	0.9900	0.5378	0.5831
8.5	0.9909	0.9823	0.5348	0.5940
9.0	0.9891	0.9873	0.5180	0.5171

Table S3. Directivity and diffraction efficiencies of three-level metasurfaces, optimized for additional wavelengths

λ_0 (μm)	Three-level (E_F = 0.2, 0.6 and 1.0 eV for +1st, 0th and -1st order, respectively)					
	Directivity (+1)	Directivity (0)	Directivity (-1)	R_{+1}	R_0	R_{-1}
7.0	0.9780	0.9317	0.9701	0.4614	0.4771	0.4408
7.5	0.9749	0.9345	0.9751	0.4723	0.4901	0.4250
8.5	0.9688	0.9468	0.9799	0.4576	0.4995	0.4743
9.0	0.9660	0.9535	0.9755	0.4462	0.5123	0.4484

S11. Performance dependence on the trade-off coefficient in FoM

In **Section 2.2** of the main text, we have set the FoM as

$$\text{FoM} = \sum_{\text{states}}(bR_{\text{target}} - \sum_{i=\text{off-target}} R_i),$$

which includes the trade-off coefficient b. To quantitatively analyze the effect of varying b on the performance of the metasurfaces, we have conducted 30 optimizations for each combination of two- and three-level metasurfaces and b = 0.1, 0.2, 0.3, 0.4, 0.5, and 0.6 (total 30 × 2 × 6 = 360 optimizations). On **Figure S8**, we report the dependence of the average directivities and average target diffraction efficiencies on the trade-off coefficient. One can observe there is a clear monotonic, conflicting trend on both quantities, making it important to choose a suitable trade-off coefficient b.

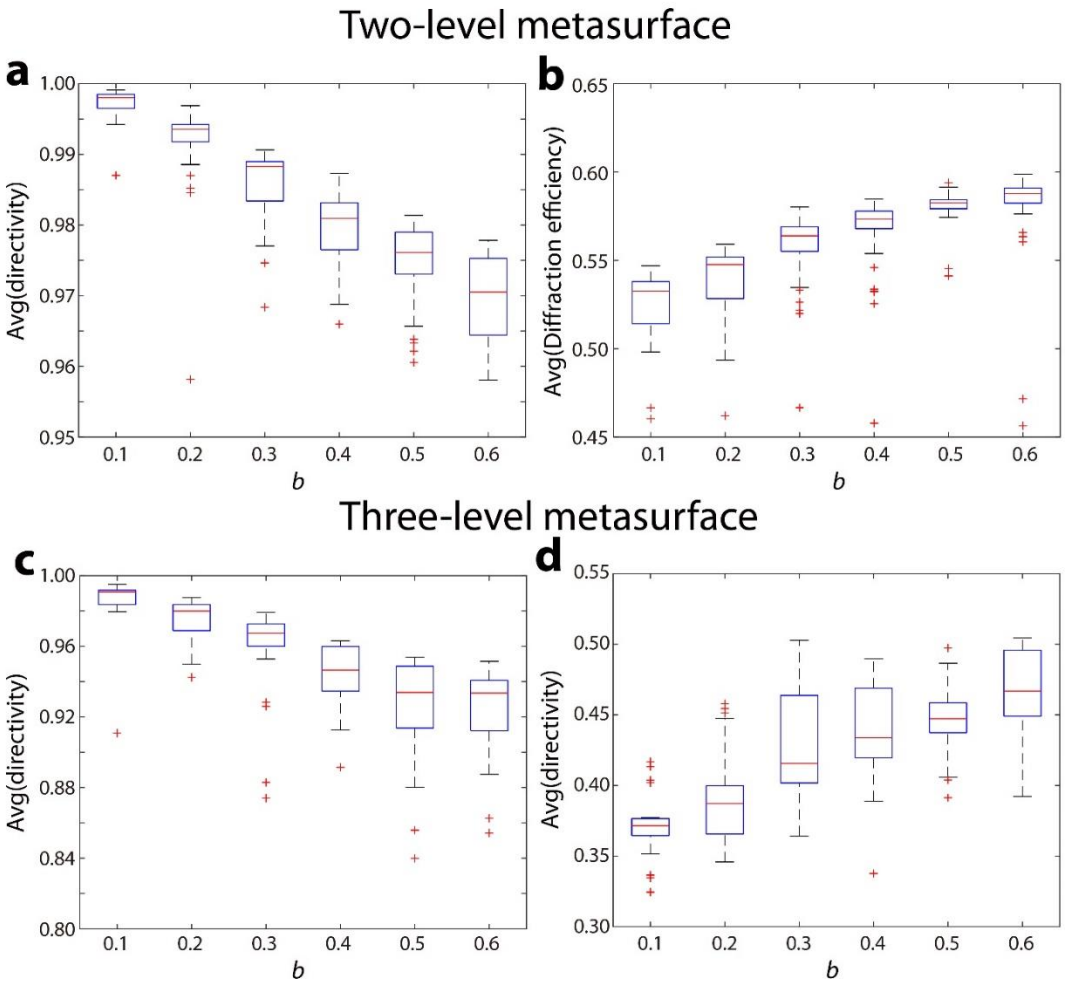

Figure S8. Average directivity and target diffraction efficiencies for **(a, b)** two- and **(c, d)** three-level metasurfaces, by varying the trade-off coefficient b. The red cross markers represent outliers.

References

[1] Das, A. *et al.* Monitoring dopants by Raman scattering in an electrochemically top-gated graphene transistor. *Nature Nanotechnology* 3, 210 (2008).

[2] Miller, O. D. *Photonic Design: From Fundamental Solar Cell Physics to Computational Inverse Design*. (University of California, Berkeley, 2012).

[3] Fante, R. L. & McCormack, M. T. Reflection properties of the Salisbury screen. *IEEE Transactions on Antennas and Propagation* 36, 1443 (1988).

[4] Sell, D. *et al.* Large-Angle, Multifunctional Metagratings Based on Freeform Multimode Geometries. *Nano Letters* 17, 3752 (2017).

[5] Falkovsky, L. A. Optical properties of graphene. in *Journal of Physics: conference series* vol. 129 12004 (2008).

[6] Fan, S. *et al.* Temporal coupled-mode theory for the Fano resonance in optical resonators. *JOSA A* 20, 569 (2003).

[7] Suh, W. *et al.* Temporal coupled-mode theory and the presence of non-orthogonal modes in lossless multimode cavities. *IEEE Journal of Quantum Electronics* 40, 1511 (2004).

[8] Alpeggiani, F. *et al.* Quasinormal-mode expansion of the scattering matrix. *Physical Review X* 7, 21035 (2017).

[9] Zschiedrich, L. *et al.* Riesz-projection-based theory of light-matter interaction in dispersive nanoresonators. *Physical Review A* 98, 43806 (2018).

[10] Binkowski, F. *et al.* Poles and zeros in non-Hermitian systems: Application to photonics. *Physical Review B* 109, 45414 (2024).